



Brittle initiation of dissolution–precipitation creep in plagioclase-rich rocks: insights from the Bergen arcs, Norway

Jo Moore^{1,2,3} · Sandra Piazzolo⁴ · Andreas Beinlich^{1,3} · Håkon Austrheim⁵ · Andrew Putnis^{1,6}

Received: 19 January 2024 / Accepted: 5 May 2024
© The Author(s) 2024

Abstract

The initiation of ductile shear zones commonly occurs spatially associated with fluid-rock reactions along brittle precursors. In many cases the relative timing of fracturing, fluid infiltration, reaction, and recrystallisation is unclear, making it difficult to disentangle mechanisms of shear zone initiation from subsequent deformation and recrystallisation. Here we present the study of the transition from a dry plagioclase-diopside-garnet-scapolite host granulite-facies lithology to (1) a low strain amphibolite-facies rock, and (2) a transition from low strain to high strain amphibolite-facies lithologies. Hydration of the granulite-facies precursor at amphibolite-facies conditions produces an assemblage comprised dominantly of plagioclase-amphibole-zoisite-clinozoisite-kyanite-scapolite-quartz. Detailed study of plagioclase chemistry and microstructures across these two transitions using Electron Backscatter Diffraction (EBSD) and Wavelength Dispersive Spectrometry (WDS) allows us to assess the degree of coupling between deformation and fluid-rock reaction across the outcrop. Plagioclase behaves dominantly in a brittle manner at the hydration interface and so the initial weakening of the rock is attributed to grain size reduction caused by fracture damage and fluid infiltration at amphibolite-facies conditions. Extensive fracturing-induced grain size reduction locally increases permeability and allows for continuing plagioclase and secondary mineral growth during shear. Based on plagioclase microstructures, such as, an inherited but dispersed crystallographic preferred orientation (CPO), truncation of chemical zoning, and the dominance of fine (5–150 µm), slightly elongate, polygonal grains we conclude that deformation is dominantly facilitated by dissolution–precipitation creep assisted by grain boundary sliding in the shear zone.

Keywords Shear localisation · Dissolution–precipitation creep · Plagioclase deformation · Brittle precursor · Amphibolite-facies · Fluid influx

Communicated by Daniela Rubatto.

✉ Jo Moore
josephine.moore@fu-berlin.de

- ¹ School of Earth and Planetary Sciences, The Institute for Geoscience Research (TIGeR), Curtin University, Perth, WA 6845, Australia
- ² Institute of Earth Sciences, University of Lausanne, Building Geopolis, UNIL-Mouline, CH-1015 Lausanne, Switzerland
- ³ Institute for Geological Sciences, Freie Universitaet Berlin, 12249 Berlin, Germany
- ⁴ School of Earth and Environment, Institute of Geophysics and Tectonics, The University of Leeds, Leeds LS2 9JT, UK
- ⁵ Physics of Geological Processes (PGP), The Njord Centre, Department of Physics, University of Oslo, P.O. Box 1048, NO-0316 Oslo, Norway
- ⁶ Institut Für Mineralogie, University of Münster, Corrensstraße 24, 48149 Münster, Germany

Introduction

It has long been recognised that shearing is commonly initiated in association with fluid infiltration on brittle precursors (Austrheim 1987; Austrheim and Griffin 1985; Pennacchioni and Mancktelow 2007; Segall and Simpson 1986; Stünitz and Fitz Gerald 1993). One explanation for this may be that the grain size reduction necessary to allow for strain localisation is achieved by reaction between the infiltrating fluid and the brittle fractured host-rock (Berger and Stünitz 1996; Fusses and Handy 2008; Goncalves et al. 2016; Rutter and Brodie 1995). Alternatively, initial grain size reduction may occur entirely as a result of fracturing (Brander et al. 2012; Imon et al. 2004; Menegon et al. 2013; Nyman et al. 1992; Okudaira et al. 2015) and the fluid infiltration and associated fluid-rock interaction facilitates strain localisation. Which process occurs has implications for the timing of strain localisation after brittle failure and is critical for

understanding the role of fluids in determining the strength of the crust.

Both scenarios proposed in the previous paragraph are models where weakening results from a grain size reduction and the infiltration of fluid, allowing for the activation of grain size sensitive creep. The primary difference between the models is the timing and role of reaction in weakening the rock. In the first scenario, from here onwards referred to as the reactive-weakening model, weakening occurs after a significant proportion of the host rock has been reacted to a finer grained or weaker mineralogy. In this scenario, continued fluid-rock interactions should result in progressive weakening at the shear zone margin (e.g., Kaatz et al. 2023), resulting in a shear zone that is widening over time. Thus, the reactive-weakening model is consistent with models involving incrementally thickening shear zones, generally classified as type 1 shear zones (Fossen and Cavalcante 2017; Hull 1988; Means 1984). Such a scenario is described in detail by Mancktelow and Pennacchioni (2005) and Pennacchioni and Mancktelow (2007). In the second scenario, from here onwards referred to as the cataclastic model, weakening is result of mechanical grain size reduction and subsequent fluid infiltration in the fracture damage zone. In the cataclastic model any further strain accumulation will be confined to the initial damage zone and percolation or diffusion of fluid into the surrounding rock will produce an alteration halo without any further weakening. The cataclastic model of shear zone formation is consistent with type 3 shear zones of Fossen and Cavalcante (2017) and the model described by Pennacchioni and Mancktelow (2018) for small scale ductile shear zones (< 1 m thick).

Here, we investigate a larger (~ 10 m thick) ductile shear zone to determine which model is consistent with shear zone initiation. We propose that the prevalent model should be evident in the rock microstructure as in the reactive-weakening model the extent of strain should be proportional to the extent of reaction, whereas in the cataclastic model reaction and deformation will not necessarily be coupled. The outcrop that is the focus of this study, located on Radøy in the Bergen Arcs, Norway, has been described previously by Moore et al. (2019); Moore et al. (2020a); and Moore et al. (2020b). The reaction from a granulite-facies precursor assemblage of plagioclase-garnet-diopside-scapolite to an amphibolite-facies assemblage dominated by plagioclase-amphibole-zoisite-clinozoisite-kyanite-scapolite-quartz has been described in detail by Moore et al. (2020a). Two main conclusions of the previous contribution of Moore et al. (2020a) are: (1) dissolution-precipitation was the governing reaction mechanism, and (2) during the transformation from granulite-facies to low strain amphibolite-facies lithologies the dissolution and precipitation reactions were coupled at the reaction interface, while they were decoupled

during the transformation from granulite-facies to the high strain amphibolite-facies lithologies. In this contribution we investigate the relationship between reaction and deformation microstructures in more detail by combined Electron Backscatter Diffraction (EBSD) and Wavelength Dispersive Spectrometry (WDS) mapping of plagioclase in the low strain and high strain amphibolite-facies domains and the granulite precursor. By comparing plagioclase microstructures, chemistry and reaction assemblages across these lithologies we aim to establish whether reaction extent and strain are proportional and whether the difference in reaction coupling or decoupling between low and high strain amphibolite-facies domains described in Moore et al. (2020a) is indicative of the process that resulted in the shear zone formation.

Geological setting

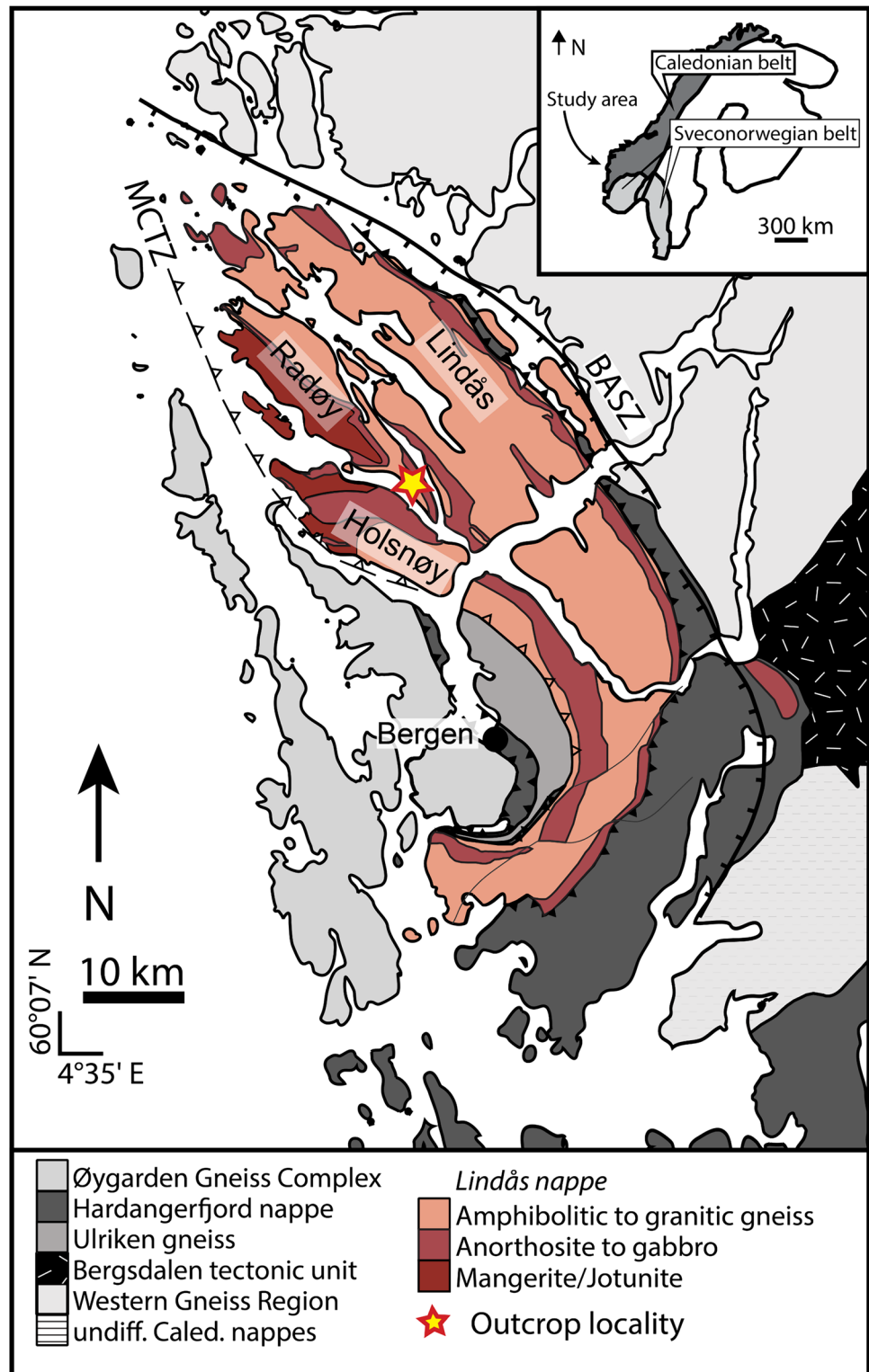
The outcrop that is the focus of this study is situated on Radøy within the Lindås Nappe of the Bergen arcs (Fig. 1). The Lindås Nappe is predominantly comprised of an anorthosite-mangerite-charnockite-granite (AMCG) suite and banded gneiss complexes. After intrusion of the AMCG suite, between 1237 ± 45 – 35 Ma to 945 ± 33 Ma (Austrheim 1990; Bingen et al. 2001), the rocks underwent granulite-facies metamorphism, between 929 Ma (Bingen et al. 2001) and 910 ± 10 Ma (Cohen et al. 1988). Following a period of quiescence, the Lindås Nappe underwent partial hydration during the Caledonian Orogeny at ~460–400 Ma (Austrheim 1987; Bingen et al. 2001; Boundy et al. 1996; Glodny et al. 2008; Kühn et al. 2002, 2020b).

Partial hydration of the previously anhydrous rocks is expressed as localised zones of both statically and dynamically metamorphosed eclogite and amphibolite-facies rocks. The outcrop presented in this study preserves static hydration of the granulite to amphibolite-facies assemblage as well as a transition from low strain to high strain amphibolite-facies lithologies. Here, static hydration of the granulite to amphibolite has been constrained to ambient temperatures of ~590–730 °C by Zr-in-rutile thermometry (Moore et al. 2020b) and pressures of 10–14 kbar based on Al-in-hornblende barometry and phase equilibrium modelling (Moore et al. 2019, 2020a), while temperatures have been estimated to have reached up to ~860 °C within the shear zone (Moore et al. 2020b).

Description of outcrop and lithologies

In this section we provide a general description of the structural characteristics of the outcrop combined with the general lithological descriptions and interpretations

Fig. 1 Study area at Radøy in the Lindås nappe of the Bergen Arcs, Western Norway. *MCTZ* Main Caledonian Thrust Zone. *BASZ* Bergen Arcs Shear Zone. Modified from Boundy, et al. (1997), Glodny, et al. (2008) and Centrella, et al. (2015)



of Moore et al. (2020a). The outcrop can be most simply described as consisting of two metamorphic facies, granulite and amphibolite (Fig. 2). The granulite, characterised as a foliated lilac-coloured mafic cluster bearing medium grained rock, is preserved as a 2–3 m wide body

encapsulated by the amphibolite lithology (Fig. 2a–c). Throughout the studied outcrop no evidence or remnants of pseudotachylite were observed. The lilac coloured plagioclase matrix comprises 70% of the volume of the granulite (Moore et al. 2020a). The remainder of the granulite

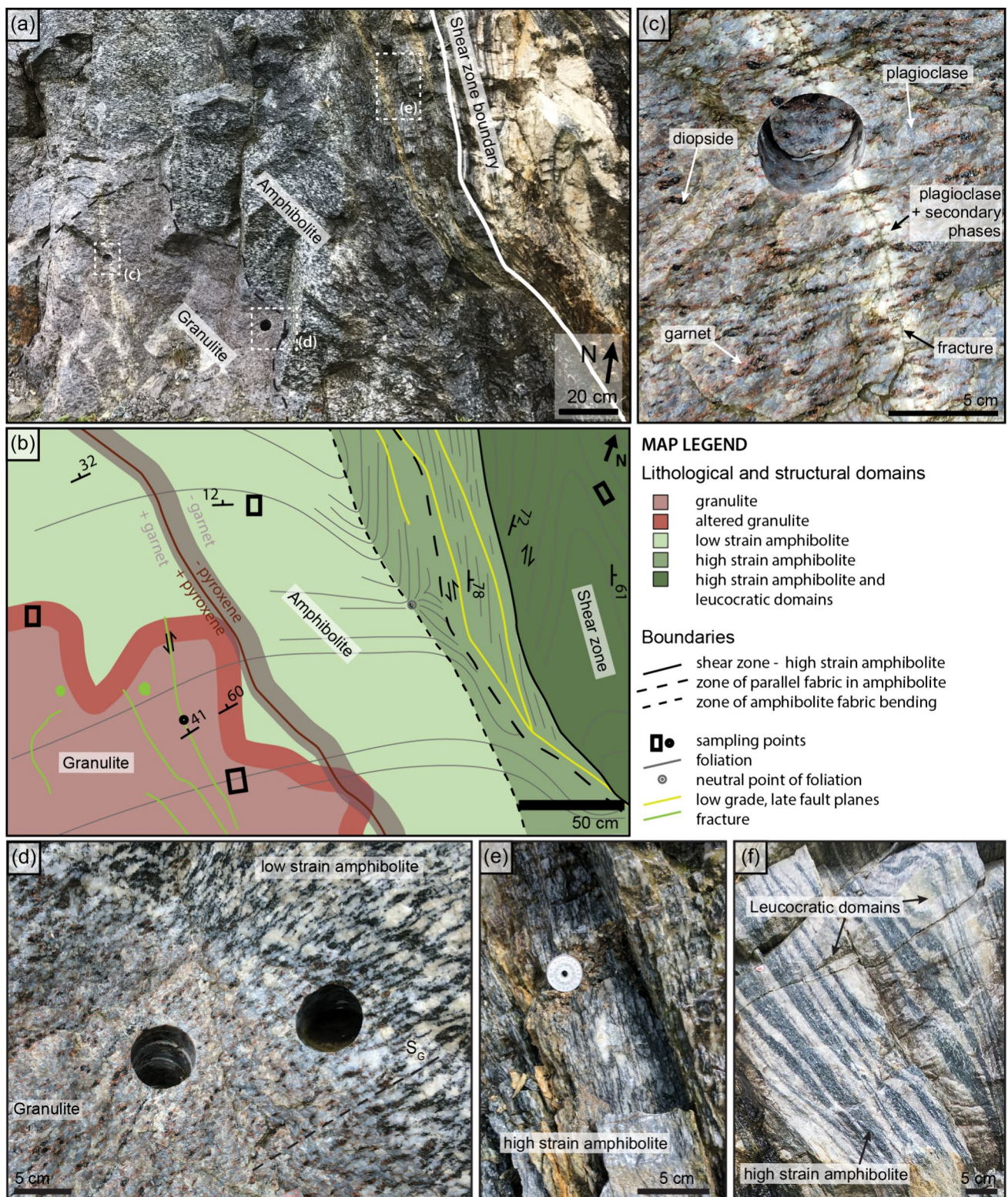


Fig. 2 Outcrop photographs (**a**, **c–f**) and map of lithological and structural domains (**b**). **a** Overview photograph of the outcrop showing the location of the granulite relative to the amphibolite and the shear zone. **b** Outcrop map detailing the mineralogical boundaries associated with hydration of the granulite at amphibolite-facies conditions and the different structural domains of amphibolite, subdivided based on degree of strain. **c** A fracture crosscutting the granu-

lite lithology, producing a milky white alteration halo in the adjacent plagioclase. **d** The granulite to amphibolite transition, the continuation of the granulite foliation (S_G) into the amphibolite is indicated by the dashed line. **e** High strain amphibolite within zone of parallel fabric. **f** Interlayering of leucocratic domains and high strain amphibolite within the shear zone

is comprised of scapolite (2%) and the foliation defining 1–2 cm elongate diopside (9%) with coronitic garnet (17%) (Fig. 2c).

Within the granulite, fractures occurring subparallel to the shear zone boundary (SZB) are observed (Fig. 2b & c). These fractures are characterised by a central 1–2 mm wide dark greenish core and 2–4 cm wide alteration halo, within which the granulitic plagioclase is milky white due to an abundance of zoisite, quartz, and kyanite \pm muscovite inclusions (Moore et al. 2020a). Mafic clusters that are crosscut by the fracture are not visibly offset (Fig. 2c), indicating that no significant displacement occurred along these small fractures.

Across the granulite to amphibolite transition, the granulite foliation (S_G) is continuous (Fig. 2b and d) with the amphibolite foliation (S_A) due to the direct replacement of diopside and garnet by amphibole. The replacement of diopside and garnet by amphibole is concomitant with the partial recrystallisation of plagioclase to finer grained aggregates containing abundant zoisite, kyanite, and quartz inclusions (Moore et al. 2020a), resulting in a milky white appearance of the plagioclase. The resulting amphibolite lithology is comprised of plagioclase (47%), amphibole (43%), zoisite (3%), kyanite (2%), and biotite (1%) with additional minor phases (Moore et al. 2020a).

At a distance of 50–100 cm to the east of the granulite to amphibolite transition, S_A bends sharply into a shear zone (Fig. 2b). This bending of S_A marks the transition from low to high strain amphibolite domains. Beyond the SZB the high strain amphibolite transitions from a zone of parallel planar fabric (Fig. 2e) into a spaced foliation defined by interlayered bands of light (leucocratic domains) and dark (high strain amphibolite) material (Fig. 2f). The shear zone extends from the SZB \sim 10 m to the northeast at which point there is no further outcropping rock.

The interlayering of leucocratic and high strain amphibolite domains in the shear zone is the result of metamorphic differentiation during hydration at amphibolite-facies (Moore et al. 2020a). Here, metamorphic differentiation associated with increasing strain results in an overall decrease in amphibole abundance. The amount of amphibole decreases from 43% in the low strain amphibolite to 18–27% in high strain amphibolite domains and 5% in leucocratic domains. The decrease in amphibole abundance with increasing strain is balanced by an increase in plagioclase and plagioclase hydration reaction products (zoisite, kyanite, and quartz \pm muscovite). Plagioclase increases in modal abundance from 47% in the low strain amphibolite to 59% in the high strain amphibolite and 74% in the leucocratic domains. Zoisite, kyanite, and quartz comprise 5% of the low strain amphibolite, 5–13% of high strain amphibolite domains and 7% in the leucocratic domains. Due to the dominance of plagioclase in the

granulite precursor lithology and the increasing abundance of plagioclase associated with increasing strain, plagioclase microstructures across the granulite – low strain amphibolite – high strain amphibolite transitions are the focus of this contribution.

Methods

Sample selection and preparation

Fracture, altered granulite, granulite, low strain amphibolite and shear zone samples were taken from the locations indicated in Fig. 2b. Thin section blocks were cut parallel to the lineation (X direction) and normal to foliation (XZ plane) present in the sample (S_G in the granulite and S_A in the amphibolite samples). Initial polishing of thin sections was followed by mechanochemical polishing with colloidal silica before they were lightly carbon coated (3–5 nm thickness) for EBSD analysis.

Quantitative analysis of mineral composition

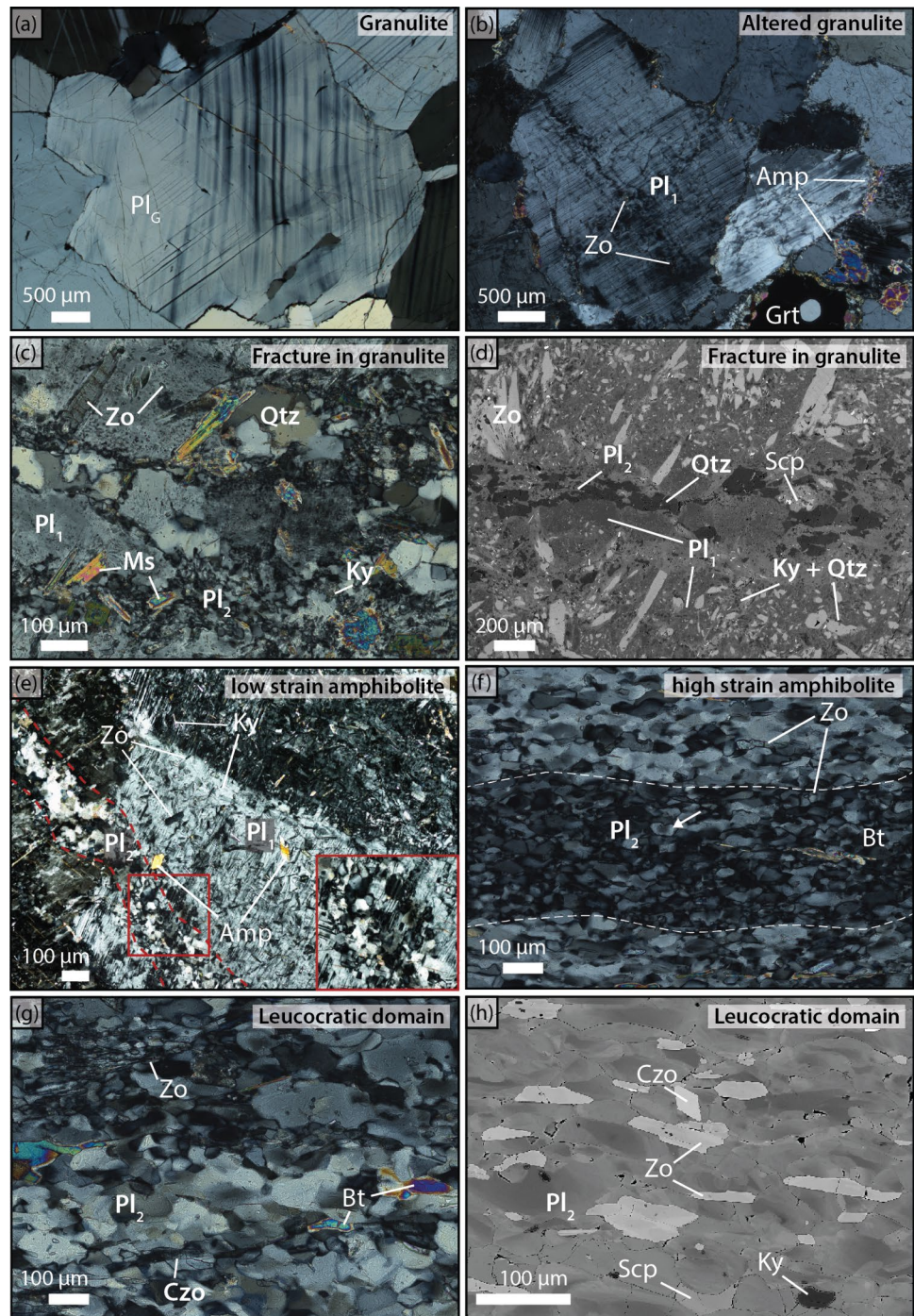
Quantitative geochemical mapping using WDS was carried out on the JEOL JXA-8530F Electron Microprobe Analyser (EMPA) at the Centre for Microscopy, Characterisation and Analysis (CMCA) at the University of Western Australia, Perth, Australia. Mapping was performed using an accelerating voltage of 15 kV, a beam current of 20 nA and spot/pixel size of 5 μ m.

Element distribution maps were acquired using the following analysing crystals: TAP for Si K α , Al K α , Na K α , and Mg K α ; PETJ for Ca K α and K K α ; and LiF for Ti K α and Fe K α . For these analyses the counting time was 20 s for all elements on each pixel. The standards employed were commercially available silicates, oxides, and metals. Mean atomic number background corrections were employed throughout (Donovan and Tingle 1996). Unknown and standard intensities were corrected for dead time and the ZAF algorithm was used for matrix absorption (Armstrong 1988). On-peak interference corrections were applied as appropriate (Donovan et al. 1992).

Quantification of grain size and crystallographic orientation relationships

EBSD analysis was carried out on the Mira3 variable pressure Field Emission Scanning Electron Microscope (FE-SEM) at the John de Laeter Centre (JdLC), Curtin University, Perth, Australia. Patterns were acquired with Symmetry EBSD detector and indexed with AzTec Synergy software (Oxford Instruments). The FE-SEM was run at a high vacuum with an accelerating voltage of 25 kV and a

Fig. 3 Cross-polarised photomicrographs and Backscattered Electron (BSE) images displaying the textural evolution of plagioclase across the hydration and deformation transitions. **a** Relatively strain-free clear plagioclase (Pl_G) in the granulite exhibiting two sets of twins. **b** Heavily fractured plagioclase (Pl_1) at the granulite-amphibolite transition hosting abundant zoisite inclusions and alteration assemblages at grain boundaries. **c** Fractures through plagioclase (visible in outcrop, see; Fig. 2b–c) hosting fine-grained secondary plagioclase (Pl_2) and amphibolite assemblage minerals. **d** BSE image showing the reaction assemblage associated with fracturing in plagioclase. **e** Plagioclase (Pl_1) in the low strain amphibolite, while highly altered, preserves the orientation of precursor grains and is intersected by bands of fine-grained polygonal plagioclase (Pl_2), outlined by red dashed lines. The inset red box is a zoom-in of the Pl_2 band. **f** In the high strain amphibolite orientation inheritance from Pl_G remains evident in Pl_2 . However, areas representative of previous grains form highly elongate discontinuous lenses. **g** Pl_2 in the leucocratic domains of the shear zone. **h** BSE image further demonstrating the relationship between Pl_2 and the hydration reaction assemblage. For (f, g and h) the foliation (SA) is parallel to the long axis of the image



beam current of 8 nA. The samples were tilted to 70° and analysed at a working distance of 20–25 mm.

EBSD data was processed using HKL's Channel 5 software. Non-indexed solutions were replaced by the most common neighbour orientation to reduce data noise following the procedure tested by Bestmann and Prior (2003); Piazzolo et al. (2006); and Prior et al. (2002). Following processing, the MTEX toolbox for Matlab (Bachmann et al. 2010) was used to produce orientation

distribution functions (ODFs) and texture index (M-index) values (Mainprice et al. 2015; Skemer et al. 2005).

A table summarising the area size, step size used and phase assemblages of the areas mapped by EBSD for calculation of grain size and plagioclase crystallographic orientation datasets is provided in the supplementary material (Table S1). A step size of 2–2.5 μm and a minimum size of 10 pixels was used for grain size, misorientation and orientation analysis for most of the amphibolite-facies

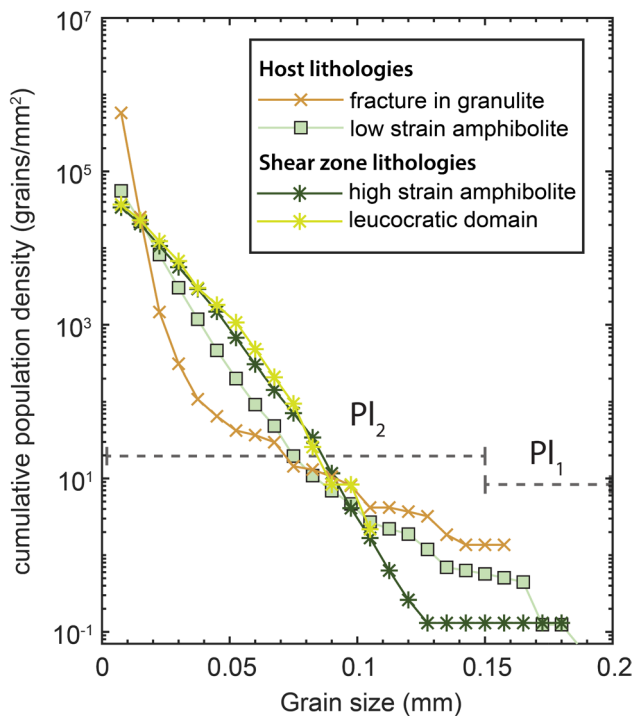


Fig. 4 Cumulative grain size (grain diameter) population density of plagioclase in the amphibolite-facies lithologies. Pl_2 exhibits increasing mean grain size and dispersion in the shear zone lithologies

samples, equating to a minimum grain diameter of 7.1–8.9 μm . For the granulite-facies samples a step size of 10 μm and a minimum size of 10 pixels was used. Grain size distributions are plotted in accordance with Cashman and Ferry (1988).

Results

Microstructural evolution of plagioclase across the outcrop

The aim of this section is to describe the textural evolution of plagioclase across the granulite – low strain amphibolite – high strain amphibolite transitions (Figs. 2 and 3). The microstructural classifications of granulitic (Pl_G) and secondary plagioclase (Pl_1 and Pl_2) are defined in this section and will be utilised throughout the remainder of this contribution.

Pl_G are medium-sized (500 μm – 5 mm, average; \sim 1.5 mm), typically optically clear grains with uniform extinction, two intersecting sets of twins, and minor alteration along grain boundaries and few fractures (Fig. 3a). Pl_1 is characterised as highly irregularly shaped substructured grains, up to 200 μm in diameter (Fig. 4), with abundant zoisite and kyanite inclusions and partially retained Pl_G

twin orientations (Fig. 3e). Pl_2 is characterised by rounded to polygonal grains with zoned extinction (Fig. 3f–h) and a variable but fine grain size (5–150 μm ; Fig. 4).

In the altered granulite Pl_1 is the dominant plagioclase microstructure. Pl_G twinning remains evident despite grains containing a high density of zoisite inclusions (Fig. 3b). Zoisite inclusions are particularly concentrated around intragranular fractures and grain boundaries (Fig. 3b), where plagioclase becomes optically turbid. Micron-scale patchy extinction of the plagioclase around fractures and inclusions (Fig. 3b) indicates partial grain size reduction of plagioclase, marking the transformation from Pl_G to Pl_1 .

Around fractures in the granulite there are two secondary plagioclase microstructures evident, Pl_1 and Pl_2 (Fig. 3c and d). Pl_1 occurs adjacent to fractures, is optically turbid, and hosts abundant zoisite and kyanite inclusions (Fig. 3c and d). In fractures crosscutting Pl_1 , Pl_2 forms bands of abundant fine (< 50 μm) to very fine (5–20 μm) grains (Fig. 4).

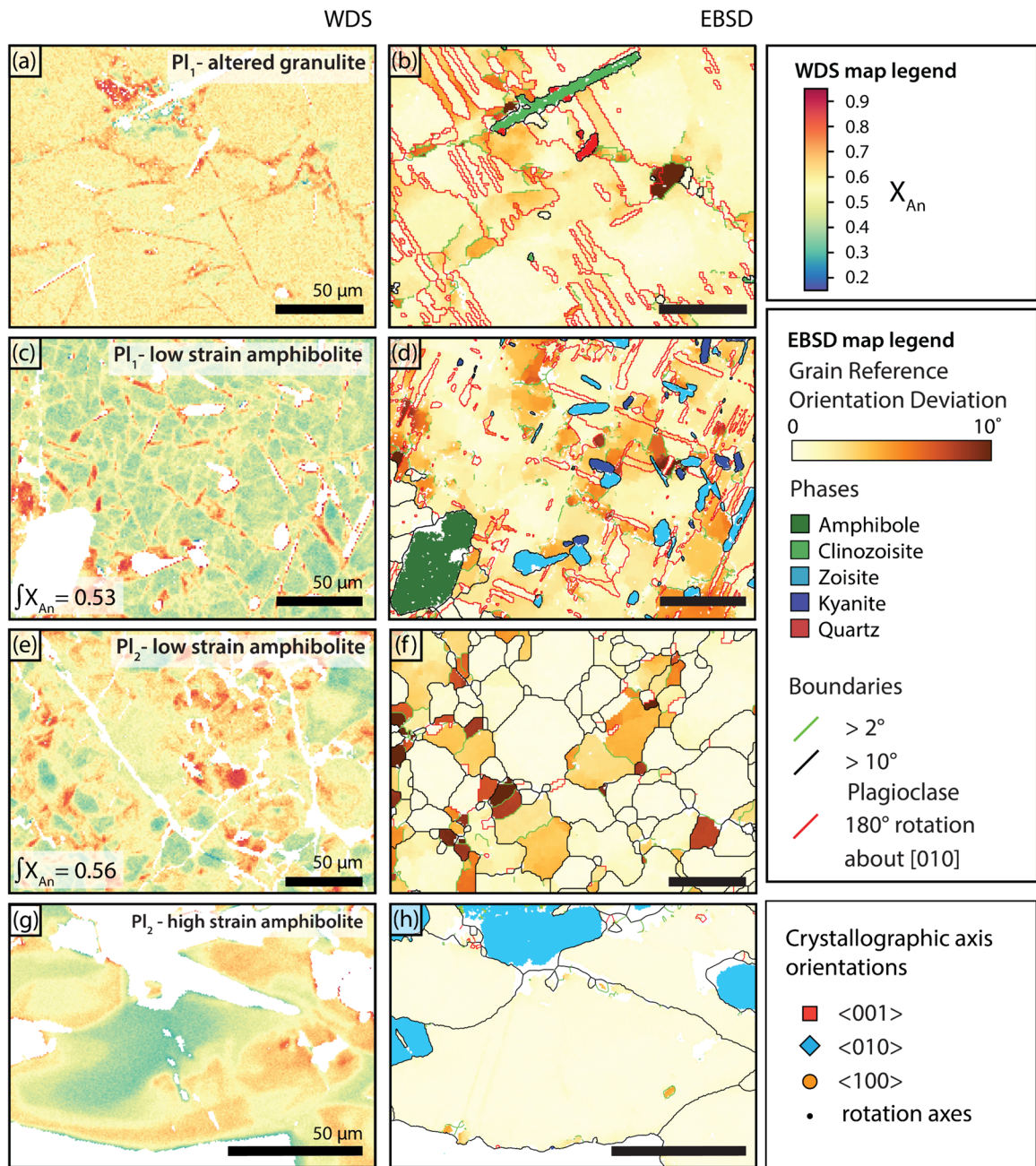
In the low strain amphibolite, there are again two secondary plagioclase microstructures evident, Pl_1 and Pl_2 . Pl_1 is the dominant plagioclase microstructure in the low strain amphibolite while Pl_2 is locally evident, forming bands of abundant fine (< 50 μm) grains (Fig. 4) that crosscut Pl_1 (Fig. 3e).

In the high strain amphibolite and leucocratic domains (Fig. 3f–h) Pl_1 is no longer present (Fig. 4). Pl_2 , while still polygonal, forms bands dominated by 50 – 150 μm grains (Fig. 4) that are elongate parallel to the foliation (Fig. 3f–h). In cross-polarised light images, inheritance of Pl_G orientation by Pl_2 are evident within the shear zone (Fig. 3f), marked by distinct elongate lensoidal bands of Pl_2 with similar extinction, indicating some precursor plagioclase grain control on orientation.

Relationship between plagioclase chemistry and microstructure

Combined WDS (Fig. 5a, c, e, g) and EBSD (Fig. 5b, d, f, h) analyses of Pl_1 and Pl_2 microstructures are presented to examine the spatial relationship between reaction and microstructure (Fig. 5). Plagioclase composition in WDS maps (Fig. 5a, c, e, g) is expressed in terms of anorthite content (X_{An}). Additionally, mineral orientations are examined to determine whether the precursor Pl_G has any crystallographic relationship with secondary Pl_1 and Pl_2 (Fig. 6).

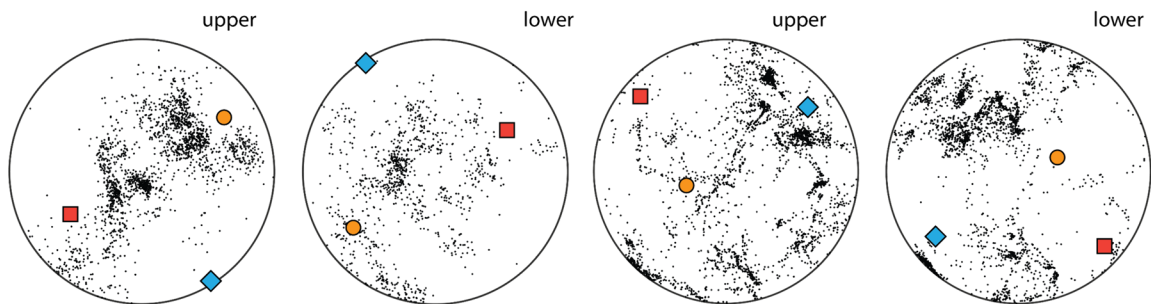
In the altered granulite, Pl_G is partially transformed to Pl_1 . The composition of plagioclase in the altered granulite is mostly uniformly close to the Pl_G composition (Pl_G X_{An} = 0.58) (Fig. 5a). Transformation from Pl_G to Pl_1 is marked by the occurrence of “complex” feldspar zoning, as described by Mukai et al. (2014). Here, complex zoning in Pl_1 is reflected by compositional variations between X_{An} = 0.45 and X_{An} = 0.8 that are associated with inclusions,



Rotation axes (2-5°) for Pl_1 in

(i) altered granulate

(j) low strain amphibolite



◀**Fig. 5** Pl_1 and Pl_2 chemistry and microstructure represented in anorthite component (X_{An}) WDS maps (a, c, e, and g) and EBSD Grain Reference Orientation Deviation (GROD) maps (b, d, f, and h). The average X_{An} is indicated in (c) and (e). Upper and lower hemisphere plots of rotation axes associated with subgrain boundaries in Pl_1 for the altered granulite and amphibolite (i–j) are representative of map areas a–b and c–d, respectively. The orientation of the $\langle 001 \rangle$, $\langle 010 \rangle$, and $\langle 100 \rangle$ axes of the host Pl_1 are indicated by coloured symbols. For GROD maps the reference orientation is the mean orientation of the grain

twin boundaries, discontinuous subgrain boundaries and discrete planes of misorientation visible in Grain Reference Orientation Deviation (GROD) maps (Fig. 5b). The average composition for the Pl_1 map area of $X_{An} = 0.53$ (Fig. 5c) indicates that there is no addition of external Ca during the reaction from Pl_G to Pl_1 . Ca-enrichment associated with inclusions and subgrain boundaries is thus balanced by Ca-depletion in the substructure and inclusion free areas in Pl_1 . A high density of substructuring within Pl_1 is further evidenced in the EBSD maps of fractures in the granulite (Fig. 6b and c). Subgrain boundaries are not associated with gradual lattice bending as indicated by the single uniform orientation of Pl_1 grains (Fig. 6b and d). Further, the rotation axes of subgrain boundaries in Pl_1 do not coincide with any of the rotation axes of the main slip systems known for plagioclase (Fig. 5i).

In Pl_1 of the low strain amphibolite, areas of decreased $X_{An} \approx 0.3$ – 0.5 occur within a network of intersecting planes of increased $X_{An} \approx 0.6$ – 0.8 (Fig. 5c). Secondary phases (i.e., zoisite, quartz, and kyanite; Fig. 5b) are commonly associated with these areas of X_{An} enrichment. In the low strain amphibolite, planes of increased X_{An} in Pl_1 again appear coincident with subgrain boundaries and discrete planes of misorientation (Fig. 5d). As in the altered granulite, subgrain boundaries in Pl_1 of the low strain amphibolite are largely discontinuous and 2 – 5° rotation axes do not coincide with any of the rotation axis of the main slip systems known for plagioclase (Fig. 5j). Relict Pl_G twin boundaries are largely overprinted (Figs. 3d and 5d).

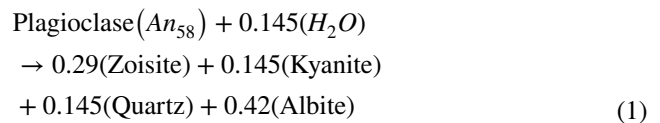
In the low strain amphibolite, Pl_2 exhibits significant intragranular compositional variation ranging between $X_{An} = 0.2$ and $X_{An} = 0.9$ (Fig. 5e). In some instances, Pl_2 grains exhibit clear concentric reverse zoning (e.g. $X_{An} = 0.2$ core and $X_{An} = 0.9$ rims). However, Pl_2 grains also commonly exhibit discontinuous enriched areas and may lack low X_{An} cores. Pl_2 in all lithologies are typically substructure-free grains (Figs. 5f, h and 6c). Further, grain and subgrain boundaries show no spatial correlation with compositional variations in Pl_2 (Fig. 5e–h). This is further evident in the high strain amphibolite, where large variations in X_{An} (0.25–0.9) are observed in the absence of substructuring and zonation is truncated by grain boundaries (Fig. 5g and h).

Around fractures and in the static amphibolite, a large proportion of Pl_2 [100]- and [010]-axes orientations are consistent with the orientation of host Pl_1 grains (Fig. 6d, f, and g). However, some dispersion is observed, resulting in a “local” CPO. In both the fracture and the amphibolite up to 60° of dispersion of Pl_2 orientations away from the host Pl_1 occurs.

Relationship between plagioclase fabric and reaction extent

In this section representative areas depicting individual original Pl_G grains across the outcrop are described for the purpose of comparing changes in fabric, shape, and degree of reaction across the granulite to low strain amphibolite to high strain amphibolite transitions (Fig. 7).

The degree of plagioclase hydration is approximated for each lithology using the following reaction.



This reaction is a simplification, particularly given the complex plagioclase compositions that are associated with the amphibolite-facies reaction (Fig. 5). However, given that zoisite is a hydrous phase that is always spatially associated with the modification of plagioclase composition (e.g., Fig. 3d and h) we consider a reaction involving zoisite to be the best proxy for calculating the extent to which the hydration reaction has affected plagioclase. Using this reaction and Pl_G and zoisite molar volumes, the amount of plagioclase required to produce the amount of zoisite in the amphibolite-facies can be estimated. This estimation is here called the reaction extent and is reported as a percentage of plagioclase (Pl_G) needed to produce the amount of zoisite locally present. For the exact method of calculation and the data shown in Fig. 7(i–ii) see Table S2.

The reaction extent is compared with the M index (misorientation index; Skemer et al. 2005) of individual plagioclase clusters in Fig. 7(ii). The M index is a measure of fabric strength, based on the difference between the observed distribution of random-pair misorientation angles and the theoretical random distribution of random-pair misorientation angles (Fig. 7(iii)). Thus, a random fabric will have an M index of 0 and a single crystal will have a M index close to 1.

Pl_G in the granulite has experienced only minor amounts of hydration ($< 1\%$) and generally has a low aspect ratio (~ 1 – 2) and little internal deviation in orientation (Figs. 5; 7a (i–ii; M index = 0.9)). The reaction extent of individual clusters of plagioclase examined in the low strain amphibolite varies from < 1 – 5% (Fig. 7(ii)). In the low strain amphibolite

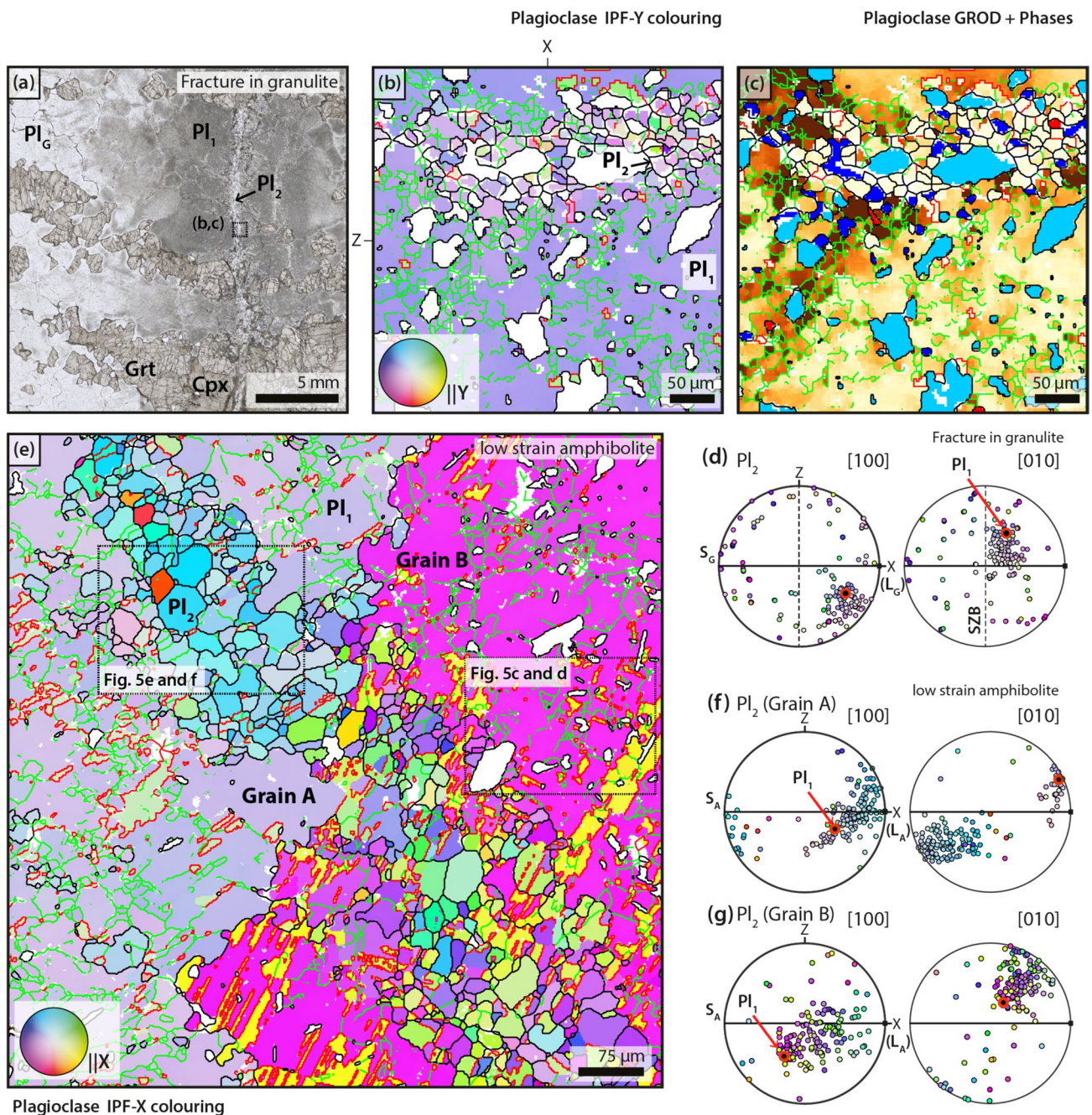


Fig. 6 Orientation relationships of secondary plagioclase assemblages occurring along fractures in Pl_G and in the amphibolite. **a** Plane-polarised photomicrograph of a fracture in granulite with indication of location for the EBSD maps shown in **(b)** and **(c)**. **b** EBSD map of plagioclase with Inverse Pole Figure (IPF-Y) colouring, depicting Pl_2 orientation within the fracture. **(c)** GROD map of plagioclase showing the distribution of low-degree disorientations within individual Pl_1 grains. Other phases are coloured according to the phase identified (for colour coding; see EBSD legend in Fig. 5). Equal area lower hemisphere pole Figures **(d)** comparing the

orientations of substructured plagioclase (Pl_1) with polygonal plagioclase (Pl_2) in map area **(b)** and **(c)**. **e** EBSD map of plagioclase in the amphibolite with IPF-X colouring. Equal area lower hemisphere pole Figures **(f)** and **(g)** comparing the orientation of substructured plagioclase (Pl_1) with polygonal plagioclase (Pl_2) in map area **(d)**. For GROD maps the reference orientation is the mean orientation of the grain. For EBSD maps, phases, boundaries, and GROD are coloured according to the legend given in Fig. 5. EBSD maps shown in **b** and **c** are rotated 90° in respect to the photomicrograph shown in **(a)**

clusters of Pl_1 , which exhibit a similar orientation, have aspect ratios in the same range as Pl_G (~1–2; Fig. 7b), a restricted local orientation spread (M index = 0.92; Fig. 7b (i)), and a reaction extent of 5%. The orientation spread of Pl_1 alone is only slightly weaker than that of Pl_G , which is consistent with a single crystal orientation with minor spread due to slight misorientations between small areas (cf. Fig. 6c). Clusters of Pl_1 and Pl_2 have aspect ratios like that of Pl_G (~1–5; Fig. 7c). However, compared to isolated Pl_1 clusters, combined Pl_1 and Pl_2 areas exhibit a considerably weaker fabric strength (M index = 0.46–0.82; Fig. 7 (i)) and a lesser reaction extent (0.4–2.3%; Fig. 7(ii)).

The reaction extent of plagioclase in the shear zone lithologies is highly variable, ranging from 1–3% in the high strain amphibolite (Fig. 7d(ii)) to 4–65% in the leucocratic domains (Fig. 7e(ii)). While Pl_2 clusters have in general a higher aspect ratio (4.5–13) their fabric is weaker (M index = 0.24–0.57; Fig. 7(i)), and there appears to be no systematic relationship between reaction extent and the aspect ratio or fabric strength of Pl_2 in the shear zone lithologies.

The dispersion of crystal orientations in Pl_2 clusters relative to Pl_G grains, as represented by the M indexes, is further demonstrated in the misorientation angle distributions (MAD) (Fig. 7(iii)). The random pair misorientation distribution for Pl_1 exhibits a single strong peak at low angles (~10–30°). For areas representing a combination Pl_1 and Pl_2 there are two weaker peaks, one at low angles (~10–40°) and one at high angles (~150–180°). Finally, in Pl_2 there are two broad peaks around low-moderate (~20–80°) and high (~130–180°) angles.

Comparison of bulk plagioclase fabric

Pole plots of plagioclase orientations shown in Fig. 8 exhibit all acquired points, sampled from the EBSD map data at 10 μm intervals, so that the data is equivalently area-fraction weighted for each of the samples. This approach enables an area-weighted comparison of the strength and characteristic of all indexed plagioclase orientations in the granulite versus the shear zone rocks, allowing for an assessment of the change in the overall difference in plagioclase fabric strength between the two lithologies. In addition, orientation data has been rotated so that it is plotted in respect to the SZB, to allow for easy comparison between samples.

Based on 235 individual Pl_G grains, plagioclase in the granulite does not exhibit a clear CPO when contoured at a halfwidth of 10° (Fig. 8a(i)) even though some CPO is seen for (001). Plagioclase orientation data in the shear zone lithologies represents 45 clusters of Pl_2 , each cluster is interpreted to reflect an individual precursor Pl_G grain. When the granulite plagioclase data is smoothed, the smoothed (20° halfwidth) orientations exhibit a similar fabric to Pl_2 of

the shear zone lithologies (Fig. 8a(ii) and b). Both exhibit weak (010)-plane maxima subparallel to the SZB and weak (001)-plane maxima at 30–70° to the SZB, however the bulk CPO in the shear zone is weaker.

Discussion

Brittle fracturing and replacement of Pl_G

Previous work on the textural and mineralogical associations of this outcrop has established that the reaction from Pl_G to Pl_1 is accomplished primarily via interface-coupled dissolution–precipitation reactions at ca. 720 °C and 10–14 kbar (Moore et al. 2020a). This interpretation is supported by the observation of microstructures in Pl_1 that are typical of dissolution–precipitation such as the inheritance of crystallographic orientation (Fig. 6d), discontinuous subgrain boundaries, and inconsistency between 2–5° rotation axes and plagioclase crystallographic axes directions (Fig. 5b, d) (Spruzeniece et al. 2017).

The brittle behaviour of Pl_G associated with fracturing is evidenced by the shared orientation of Pl_1 grains on either side of the fracture and fragment-like Pl_1 included within the fracture plane (Fig. 6a–c). Calcium enrichment along subgrain boundaries and discrete lines of misorientation in Pl_1 (Fig. 5a–d) is consistent with previous observations of annealed brittle fractures in plagioclase (Petley-Ragan et al. 2020; Petley-Ragan et al. 2018; Pittarello et al. 2008). Therefore, we infer a strong association between fracturing and reaction during the transformation of Pl_G to Pl_1 . This brittle behaviour of Pl_G may also explain the orientation inheritance exhibited by Pl_2 (Figs. 6 and 7). If Pl_G underwent comminution during fracturing, the resulting grain fragments may have acted as seeds for growth of Pl_2 .

Deformation mechanism in the shear zone

The following observations, consistent with previous work (Marti et al. 2018; Mukai et al. 2014; Stünitz et al. 2020), support dissolution–precipitation creep as the primary mechanism for Pl_2 deformation in the shear zone lithologies:

1. A weak to random CPO of Pl_2 in the shear zone (Fig. 8b) that is unfavourably oriented for slip on the dominant plagioclase slip system ((010) < 001 >; Ji and Mainprice 1988; Kruse et al. 2001; Stünitz et al. 2003; Svahnberg and Piazzolo 2010), and is not apparently related to the kinematic framework defined by the foliation and lineation.
2. Grains show very little systematic internal orientation changes (Figs. 5b, d and 6d), which would be expected if

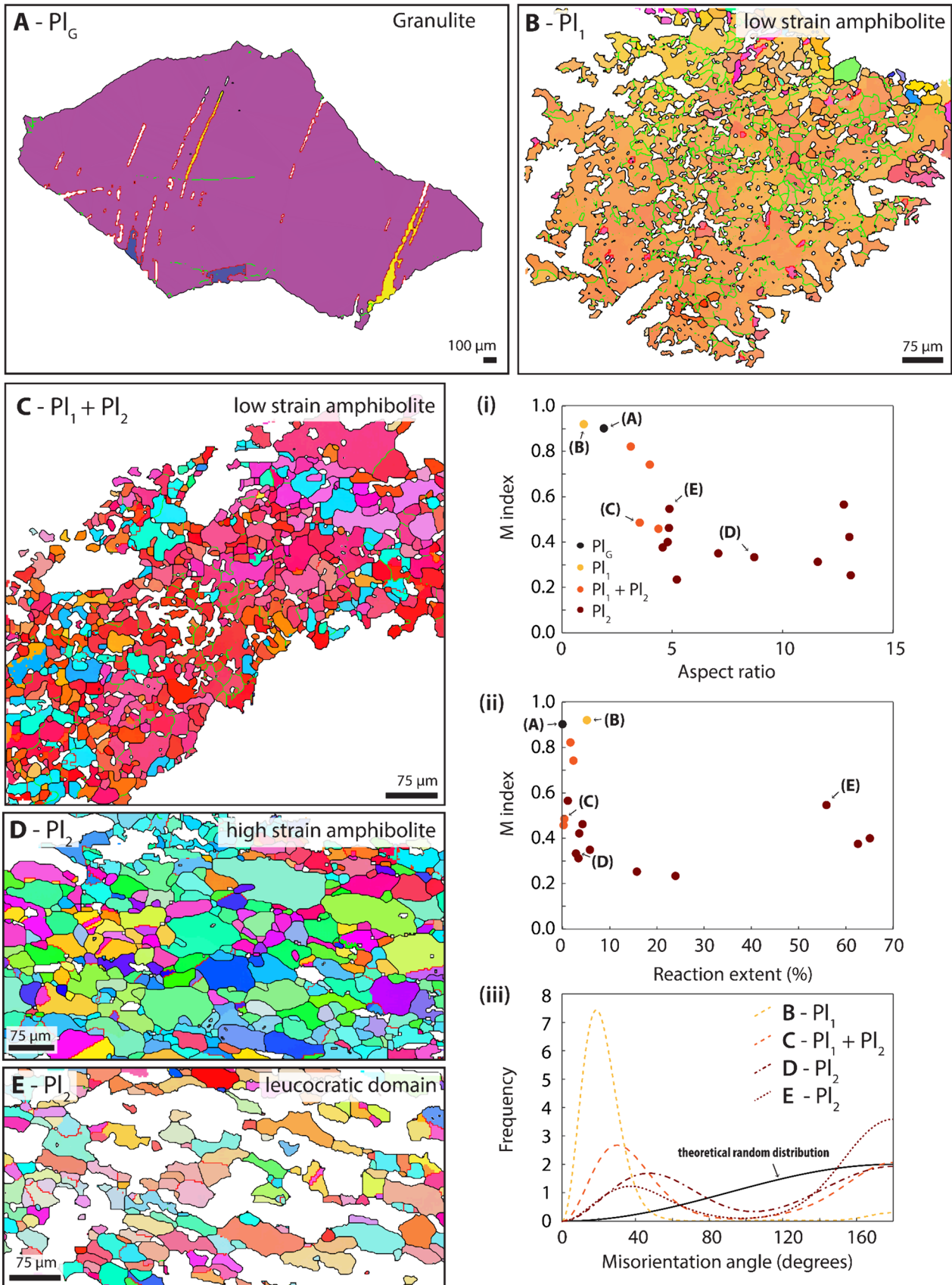


Fig. 7 Evolution of areas representing a single original Pl_G grain across the hydration-deformation transition. (A–E) IPF-Y coloured plagioclase EBSD maps displaying representative overall grain shape and orientation relationships for each of the plagioclase microstructures. (i) Plot of local M texture index against the aspect ratio of the area now representing a single original Pl_G grain. (ii) Plot of local M texture index against the reaction extent of the area representing a single original Pl_G grain. Reaction extent is calculated as the approximate percentage of precursor plagioclase needed to produce the secondary phases now present in each sample. Random-pair misorientation angle distribution (iii) for mapped areas (B–E). For EBSD maps, orientations and boundaries are coloured according to the legend given in Figs. 5 and 6

dislocation creep was dominant (e.g., Kruse et al. 2001; Svahnberg and Piazzolo 2010).

3. Truncation of the Pl_2 anorthite zoning by grain boundaries oriented parallel to the shear zone (S_A) foliation (Fig. 5g), suggesting preferential dissolution of Pl_2 grains parallel to the principal shortening axis.
4. The polygonal, slightly elongate (Fig. 7d and e), shape and small grain size (5–150 μm) of Pl_2 grains in the shear zone lithologies (Fig. 3f, g), allowing for a grain size-dependent creep mechanism, such as dissolution–precipitation creep, to be dominant. Here, we suggest another potential microstructural indicator of dissolution–precipitation creep in plagioclase:
5. The preservation of distinct bands of similar orientation representing parent plagioclase (Pl_G) grains. In this instance, resulting in a weak inherited CPO in elongated Pl_2 clusters of shear zone lithologies (Figs. 6 and 7).

This microstructure has previously been attributed to diffusion creep assisted by grain boundary sliding at greenschist-facies conditions (Jiang et al. 2000; Wheeler et al. 2001). Those authors also observe a weakening of fabric and a shift in the MAD peak towards higher angles within individual parent grain domains with increasing strain (Fig. 7(ii)), supporting progressive dispersion of crystal axes by a grain boundary sliding mechanism. Grain boundary sliding evident here by both the dispersion of fabric within Pl_2 clusters representing original Pl_G grains and the dominance of small, polygonal grains in the shear zone lithologies (Fig. 7). However, we favour a dissolution–precipitation rather than diffusion creep mechanism as the increase of hydration reaction products with strain (Fig. 7(i)) indicates that deformation occurred in the presence of fluid. Consequently, identifying the dominant mechanism as dissolution–precipitation creep, which is a mechanism that is enabled by the presence of grain boundary fluid, as the appropriate mechanism is more appropriate than the use of the generalised diffusion creep term.

Therefore, the Pl_1 microstructure in the low strain amphibolite represents dissolution–precipitation reaction without shear localisation (i.e., the hydration transition) while Pl_2 in the high strain amphibolite and shear zone lithologies

represents reaction with shear localisation (i.e., the deformation transition) and successive dissolution–precipitation creep assisted by grain-boundary sliding. In the following, the plagioclase microstructures across the hydration–deformation transitions are discussed to determine which are the important factors for determining the occurrence of shear localisation.

Shear zone initiation

In our previous work (Moore et al. 2020a) we suggested that two reaction zones can be distinguished at the hydration transition based on reaction textures and calculated H_2O activity for the mineral assemblages: type 1 zones exhibit limited permeability and thus limited mass transport, and type 2 zones are characterized by high permeability and thus enhanced mass transport.

In type 1 zones reactions proceed by near pseudomorphic replacement of the granulite-facies assemblage by the amphibolite-facies assemblages, such as the replacement of Pl_G by Pl_1 (e.g., Fig. 3b). Pseudomorphic reaction textures indicate that the dissolution and precipitation steps of the reaction remained coupled at the grain-scale reaction interface (Putnis 2002, Putnis et al. 2005). Further, the observed orientation inheritance of Pl_1 replacing Pl_G (Fig. 6b and d) is consistent with an interface-coupled reaction mechanism. It has been demonstrated that where a crystallographically compatible host phase is present, the coupling of the dissolution and precipitation reaction steps at the interface allows for crystallographic information to be transferred from the parent to the product (Putnis et al. 2005; Ruiz-Agudo et al. 2014; Spruzeniec et al. 2017; Xia et al. 2009). However, the replacement is not always perfect, hence misorientations develop during such replacement reactions resulting in orientations that are slightly dispersed relative to the crystallographic orientation of the original grain (Spruzeniec et al. 2017). In this case, rotation axes are not related to specific slip systems, and are near random (e.g., Fig. 5i). Hydration reactions in low permeability zones (type 1 zones) thus occur predominantly via interface-coupled dissolution–precipitation reactions. In this study low permeability zones are represented by lithologies dominated by Pl_1 , such as the low strain amphibolite.

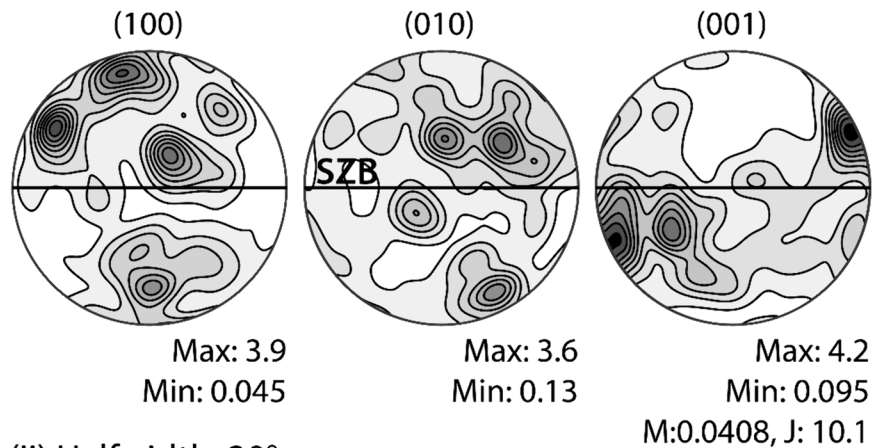
By contrast, amphibolite-facies minerals within intergranular fractures (e.g., Fig. 6a–c) and leucocratic domains of the shear zone are inferred to represent type 2 zones where dissolution and precipitation steps are decoupled allowing for mass transport at least at the grain scale (Moore et al. 2020a). As a result, reaction sites of dissolution and precipitation are not the same. In these zones, if far-field stresses are present, dissolution surface will be at high angle to the maximum stress axis and precipitation will occur in low stress areas. In this study,

Fig. 8 Comparison of plagioclase fabric in (a) the granulite and (b) the shear zone lithologies. Pole Figures exhibit all indexed points for the given map areas, contoured at indicated halfwidths. The plagioclase pole Figures shown in A represents 235 individual Pl_G grains, while the pole Figures shown in B represent 45 Pl_2 grain clusters, where a cluster is defined as similarly oriented Pl_2 grains within close proximity to each other. Each cluster is interpreted to have originated from an individual Pl_G grain (see Fig. 6). Pole plots have been re-oriented so that the x-axis is parallel to the SZB. In the shear zone lithologies the SZB is approximately parallel to the foliation (SA)

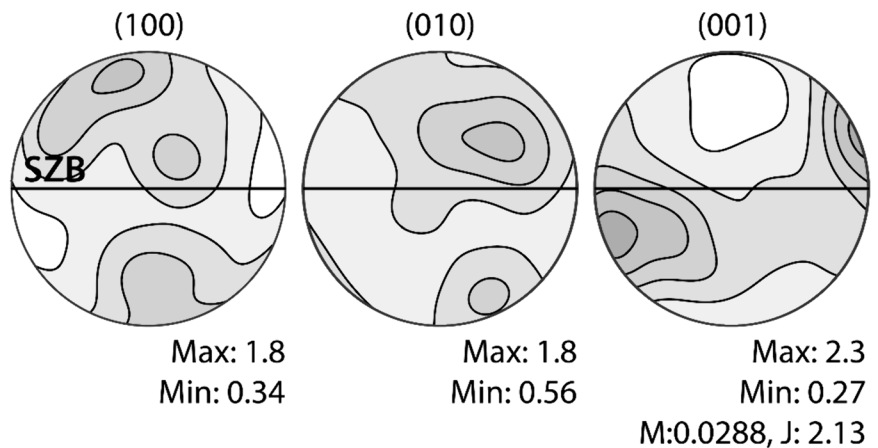
A - Pl_G in Granulite

(i) Halfwidth: 10°

Step size = $10 \mu\text{m}$, N Pl_G grains = 235
Area = 434 mm^2



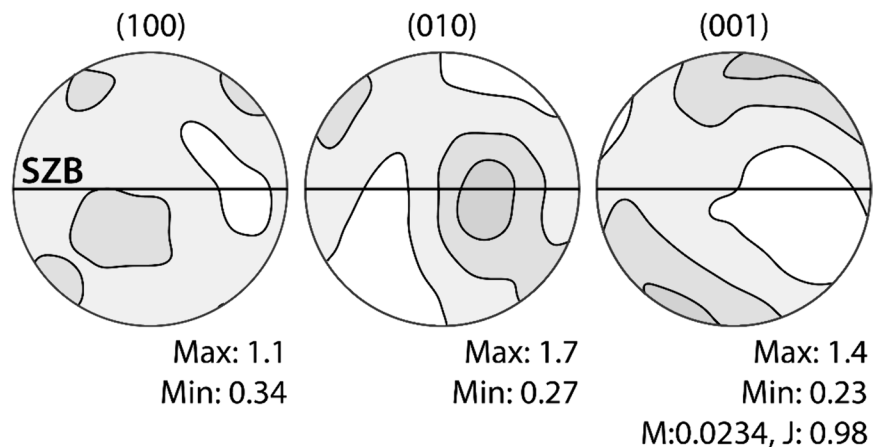
(ii) Halfwidth: 20°



B - Pl_2 in shear zone lithologies

Halfwidth: 10°

Step size = $10 \mu\text{m}$, N Pl_G grains = 45
Area = 72 mm^2



these higher permeability zones are represented by Pl_2 dominated lithologies, i.e., those occurring in the shear zone. Type 1 zones of limited permeability thus coincide with lithologies that do not undergo significant creep, while type 2 zones of high permeability coincide with zones of strain localisation. The preservation of these two contrasting reaction textures implies that comparatively low and high permeability zones were present before or during reaction. We therefore suggest that grain size reduction resulting in higher permeability and allowing for fluid infiltration and weakening occurred prior to reaction.

In addition, there seems to be no dependency between reaction extent and fabric strength or aspect ratio in plagioclase clusters in either the low strain or the high strain amphibolite (Fig. 7(i–ii)). The fact that plagioclase in the low strain amphibolite undergoes a similar degree of hydration reaction as in the shear zone lithologies (Fig. 7(i)) but does not undergo any considerable deformation, indicates that the localisation of strain is not entirely dependent on reaction extent as may be expected from the reactive-weakening model of shear zone initiation.

The inference is that Pl_2 microstructures are derived from Pl_G , dependent on the degree of damage from fracturing and syn-damage comminution, consistent with the cataclastic model of shear zone initiation. A progressive increase in Pl_2 grain size from the fractures to the statically hydrated amphibolite and then finally the shear zone lithologies is predicted to occur due to surface energy-driven grain growth (Masuda et al. 1997; Pearce and Wheeler 2011) and is in agreement with previous observations of coarsening due to growth and recrystallisation after fracture-induced fragmentation (Menegon et al. 2013). This would lead to a more pronounced polygonal microstructure (Figs. 3f, g and 5f, h) and unimodal grain size distribution (Fig. 4). In summary, our observations support an original brittle origin for Pl_2 . Syn-imbric comminution is followed by fluid influx causing reaction and surface energy-driven grain growth coupled with deformation dominated by dissolution–precipitation creep assisted by grain boundary sliding.

Thus, we propose a brittle origin for the formation of the shear zone in type 2 zones, represented by Pl_2 microstructures, consistent with previous interpretations for the formation of shear zones in the dry lower crustal rocks of the Bergen arcs (Austrheim 1987; Austrheim and Engvik 1997; Jamtveit et al. 1990). Here shear localisation in plagioclase is the result of fracturing-induced grain size reduction (Brander et al. 2012; Okudaira et al. 2015). Grain size reduction and comminution results in localized high permeability and initial fluid influx (e.g., Fusses and Handy 2008;

Menegon 2015), which allows continued reaction, growth and deformation via dissolution–precipitation creep. In contrast, type 1 zones, represented by Pl_1 microstructures, only experienced damage without comminution, allowing for fluid infiltration and reaction but not significant deformation.

Conclusions and implications

This study presents the apparent progression from plagioclase in dry, relatively undeformed anorthositic gabbro granulite to a plagioclase-rich shear zone rock that was deformed at conditions of ca. 720 °C and 10–14 kbar. The three representative plagioclase microstructures presented here represent the transformation from dry (Pl_G) to either hydrated (Pl_1) or to fine-grained sheared plagioclase (Pl_2). We observe no clear evidence for an evolution from Pl_1 to Pl_2 . The lack of clear evidence for a progression through the plagioclase microstructures and the abundance of brittle microstructures in Pl_G and Pl_1 suggests that Pl_2 is formed by the brittle fracturing of Pl_G . The formation of Pl_2 , and thus the shear zone, via comminution of Pl_G is consistent with the inherited CPO in the shear zone, suggesting Pl_G fragments acted as seeds for Pl_2 growth. The initial grain size reduction and comminution in the fracture damage zone creates a zone of higher permeability, which then allows for the infiltration of fluid and reaction. Fluid percolation and/or diffusion into the surrounding low permeability rock allows for reaction but not for the localisation of strain. Strain is localised within the area of initial high damage, consistent with the cataclastic model of shear zone formation. The shear zone morphology should thus be consistent with the morphology of the initial high damage zone.

We suggest that the following microstructures observed in Pl_2 indicate that dissolution–precipitation creep, supported by grain boundary sliding, was the dominant mechanism of deformation in the shear zone:

- Local, inherited CPO, clearly indicated by distinct bands of similar orientation representing parent plagioclase grains.
- A bulk CPO that is weak to near random, and is unfavourably oriented for both slip on the dominant plagioclase slip system ($(010) < 100 >$) and in relation to the kinematic framework.
- Fine-grained (5–150 μm), slightly elongate, polygonal grains.
- Truncation of anorthite zoning.

Such plagioclase microstructures may therefore be used to identify where shear zone formation has occurred via brittle

fracturing and subsequent dissolution–precipitation creep. In particular, the inheritance of distinct bands of similar orientation may be an important indicator of a cataclastic model of shear zone initiation.

Supplementary Information The online version contains supplementary material available at <https://doi.org/10.1007/s00410-024-02141-0>.

Acknowledgements This manuscript has benefitted greatly from the suggestions of Holger Stünitz and an anonymous reviewer. This research was funded by the Australian Research Council Discovery Project of Putnis, Raimondo, and Daczko (ARC grant number DP160103449). The authors acknowledge the facilities, and the scientific and technical assistance of the Australian Microscopy and Microanalysis Research Facility at the Centre for Microscopy, Characterisation and Analysis, The University of Western Australia, a facility funded by the University, State and Commonwealth Governments. Part of this research was undertaken using the EM instrumentation (ARC LE130100053) at the John de Laeter Centre, Curtin University.

Funding Open Access funding enabled and organized by Projekt DEAL.

Open Access This article is licensed under a Creative Commons Attribution 4.0 International License, which permits use, sharing, adaptation, distribution and reproduction in any medium or format, as long as you give appropriate credit to the original author(s) and the source, provide a link to the Creative Commons licence, and indicate if changes were made. The images or other third party material in this article are included in the article's Creative Commons licence, unless indicated otherwise in a credit line to the material. If material is not included in the article's Creative Commons licence and your intended use is not permitted by statutory regulation or exceeds the permitted use, you will need to obtain permission directly from the copyright holder. To view a copy of this licence, visit <http://creativecommons.org/licenses/by/4.0/>.

References

- Armstrong J (1988) Quantitative analysis of silicate and oxide materials: comparison of Monte Carlo, ZAF, and phi (rho-z) procedures. *Analysis Microbeam* 239–246
- Austrheim H (1987) Eclogitization of lower crustal granulites by fluid migration through shear zones. *Earth Planet Sci Lett* 81(2–3):221–232. [https://doi.org/10.1016/0012-821X\(87\)90158-0](https://doi.org/10.1016/0012-821X(87)90158-0)
- Austrheim H, Griffin WL (1985) Shear deformation and eclogite formation within granulite-facies anorthosites of the Bergen Arcs, western Norway. *Chem Geol* 50(1–3):267–281
- Austrheim H, Engvik AK (1997) Fluid transport, deformation and metamorphism at depth in a collision zone. In: *Fluid flow and transport in rocks: mechanisms and effects*, vol. Springer, pp 123–137
- Austrheim H (1990) Fluid induced processes in the lower crust as evidenced by Caledonian eclogitization of Precambrian granulites, Bergen Arcs, western-Norway. Doctoral thesis
- Bachmann F, Hielscher R, Schaeben H (2010) Texture analysis with MTEX—free and open source software toolbox. *Solid State Phenomena* 160:63–68
- Berger A, Stünitz H (1996) Deformation mechanisms and reaction of hornblende: examples from the Bergell tonalite (Central Alps). *Tectonophysics* 257(2–4):149–174. [https://doi.org/10.1016/0040-1951\(95\)00125-5](https://doi.org/10.1016/0040-1951(95)00125-5)
- Bestmann M, Prior DJ (2003) Intragranular dynamic recrystallization in naturally deformed calcite marble: diffusion accommodated grain boundary sliding as a result of subgrain rotation recrystallization. *J Struct Geol* 25(10):1597–1613. [https://doi.org/10.1016/S0191-8141\(03\)00006-3](https://doi.org/10.1016/S0191-8141(03)00006-3)
- Bingen B, Davis WJ, Austrheim H (2001) Zircon U–Pb geochronology in the Bergen arc eclogites and their Proterozoic protoliths, and implications for the pre-Scandian evolution of the Caledonides in western Norway. *Geol Soc Am Bull* 113(5):640–649. [https://doi.org/10.1130/0016-7606\(2001\)113%3c0640:ZUPGIT%3e2.0.CO;2](https://doi.org/10.1130/0016-7606(2001)113%3c0640:ZUPGIT%3e2.0.CO;2)
- Boundy TM, Essene EJ, Hall CM, Austrheim H, Halliday A (1996) Rapid exhumation of lower crust during continent–continent collision and late extension: Evidence from $^{40}\text{Ar}/^{39}\text{Ar}$ incremental heating of hornblendes and muscovites, Caledonian orogen, western Norway. *Geol Soc Am Bull* 108(11):1425–1437. [https://doi.org/10.1130/0016-7606\(1996\)108%3c1425:REOLCD%3e2.3.CO;2](https://doi.org/10.1130/0016-7606(1996)108%3c1425:REOLCD%3e2.3.CO;2)
- Boundy TM, Mezger K, Essene EJ (1997) Temporal and tectonic evolution of the granulite–eclogite association from the Bergen Arcs, western Norway. *Lithos* 39(3–4):159–178. [https://doi.org/10.1016/S0024-4937\(96\)00026-6](https://doi.org/10.1016/S0024-4937(96)00026-6)
- Brander L, Svahnberg H, Piazzolo S (2012) Brittle–plastic deformation in initially dry rocks at fluid–present conditions: transient behaviour of feldspar at mid–crustal levels. *Contrib Miner Petrol* 163(3):403–425
- Cashman KV, Ferry JM (1988) Crystal size distribution (CSD) in rocks and the kinetics and dynamics of crystallization: III. Metamorphic crystallization. *Contrib Miner Petrol* 99:401–415
- Centrella S, Austrheim H, Putnis A (2015) Coupled mass transfer through a fluid phase and volume preservation during the hydration of granulite: an example from the Bergen Arcs, Norway. *Lithos* 236:245–255. <https://doi.org/10.1016/j.lithos.2015.09.010>
- Cohen A, Onions R, Siegenthaler R, Griffin W (1988) Chronology of the pressure–temperature history recorded by a granulite terrain. *Contrib Mineral Petrol* 98(3):303–311. <https://doi.org/10.1007/BF00375181>
- Donovan JJ, Snyder DA, Rivers ML (1992) An improved interference correction for trace element analysis. In: *Proceedings of the Annual Meeting–Electron Microscopy Society of America*, vol. San Francisco press, pp 1646–1646
- Donovan JJ, Tingle TN (1996) An improved mean atomic number background correction for quantitative microanalysis. *Microsc Microanal* 2(1):1–7. <https://doi.org/10.1017/S1431927696210013>
- Fossen H, Cavalcanti GCG (2017) Shear zones—A review. *Earth Sci Rev* 171:434–455. <https://doi.org/10.1016/j.earscirev.2017.05.002>
- Fussey F, Handy MR (2008) Micromechanisms of shear zone propagation at the brittle–viscous transition. *J Struct Geol* 30(10):1242–1253. <https://doi.org/10.1016/j.jsg.2008.06.005>
- Glodny J, Kühn A, Austrheim H (2008) Geochronology of fluid–induced eclogite and amphibolite facies metamorphic reactions in a subduction–collision system, Bergen Arcs, Norway. *Contrib Mineral Petrol* 156(1):27–48. <https://doi.org/10.1007/s00410-007-0272-y>
- Goncalves P, Poilvet J–C, Oliot E, Trap P, Marquer D (2016) How does shear zone nucleate? An example from the Suretta nappe (Swiss Eastern Alps). *J Struct Geol* 86:166–180. <https://doi.org/10.1016/j.jsg.2016.02.015>
- Hull J (1988) Thickness–displacement relationships for deformation zones. *J Struct Geol* 10(4):431–435
- Imon R, Okudaira T, Kanagawa K (2004) Development of shape– and lattice–preferred orientations of amphibole grains during initial cataclastic deformation and subsequent deformation by dissolution–precipitation creep in amphibolites from the Ryoke

- metamorphic belt, SW Japan. *J Struct Geol* 26(5):793–805. <https://doi.org/10.1016/j.jsg.2003.09.004>
- Jamtveit B, Bucher-Nurminen K, Austrheim H (1990) Fluid controlled eclogitization of granulites in deep crustal shear zones, Bergen arcs, Western Norway. *Contrib Miner Petrol* 104(2):184–193. <https://doi.org/10.1007/BF00306442>
- Ji S, Mainprice D (1988) Natural deformation fabrics of plagioclase: implications for slip systems and seismic anisotropy. *Tectonophysics* 147(1–2):145–163
- Jiang Z, Prior DJ, Wheeler J (2000) Albite crystallographic preferred orientation and grain misorientation distribution in a low-grade mylonite: implications for granular flow. *J Struct Geol* 22(11–12):1663–1674
- Kaatz L, Schmalholz S, John T (2023) Numerical simulations reproduce field observations showing transient weakening during shear zone formation by diffusional hydrogen influx and H₂O inflow. *Geochem Geophys Geosyst* 24(5):e2022GC010830
- Kruse R, Stünitz H, Kunze K (2001) Dynamic recrystallization processes in plagioclase porphyroclasts. *J Struct Geol* 23(11):1781–1802
- Kühn A, Glodny J, Austrheim H, Råheim A (2002) The Caledonian tectono-metamorphic evolution of the Lindås Nappe: Constraints from U-Pb, Sm-Nd and Rb-Sr ages of granitoid dykes. *Norwegian J Geol/Norsk Geologisk Forening* 82(1)
- Mainprice D, Bachmann F, Hielscher R, Schaebe H (2015) Descriptive tools for the analysis of texture projects with large datasets using MTEX: strength, symmetry and components. *Geol Soc London Spec Public* 409(1):251–271
- Mancktelow NS, Pennacchioni G (2005) The control of precursor brittle fracture and fluid–rock interaction on the development of single and paired ductile shear zones. *J Struct Geol* 27(4):645–661. <https://doi.org/10.1016/j.jsg.2004.12.001>
- Marti S, Stünitz H, Heilbronner R, Plümper O, Kilian R (2018) Synkinematic hydration reactions, grain size reduction, and dissolution-precipitation creep in experimentally deformed plagioclase-pyroxene mixtures. *Solid Earth* 9(4):985–1009. <https://doi.org/10.5194/se-9-985-2018>
- Masuda T, Morikawa T, Nakayama Y, Suzuki S (1997) Grain-boundary migration of quartz during annealing experiments at high temperatures and pressures, with implications for metamorphic geology. *J Metamorphic Geol* 15(3):311–322
- Means W (1984) Shear zones of types I and II and their significance for reconstruction of rock history. *Geol Soc Am Bull Abstract Prog* 16:50
- Menegon LF, Florian. Stünitz, Holger. Xiao, Holger. (2015) Creep cavitation bands control porosity and fluid flow in lower crustal shear zones. *Geology* 43(3):227–230
- Menegon L, Stünitz H, Nasipuri P, Heilbronner R, Svahnberg H (2013) Transition from fracturing to viscous flow in granulite facies perthitic feldspar (Lofoten, Norway). *J Struct Geol* 48:95–112
- Moore J, Beinlich A, Austrheim H, Putnis A (2019) Stress orientation-dependent reactions during metamorphism. *Geology* 47(2):151–154
- Moore J, Beinlich A, Piazzolo S, Austrheim H, Putnis A (2020a) Metamorphic differentiation via enhanced dissolution along high permeability zones. *J Petrol*. <https://doi.org/10.1093/petrology/egaa096>
- Moore J, Beinlich A, Porter JK, Talavera C, Berndt J, Piazzolo S, Austrheim H, Putnis A (2020b) Microstructurally controlled trace element (Zr, U-Pb) concentrations in metamorphic rutile: An example from the amphibolites of the Bergen Arcs. *J Metamorph Geol* 38(1):103–127. <https://doi.org/10.1111/jmg.12514>
- Mukai H, Austrheim H, Putnis CV, Putnis A (2014) Textural evolution of plagioclase feldspar across a shear zone: implications for deformation mechanism and rock strength. *J Petrol* 55(8):1457–1477
- Nyman MW, Law RD, Smelik EA (1992) Cataclastic deformation mechanism for the development of core-mantle structures in amphibole. *Geology* 20(5):455–458
- Okudaira T, Jeřábek P, Stünitz H, Füsseis F (2015) High-temperature fracturing and subsequent grain-size-sensitive creep in lower crustal gabbros: evidence for coseismic loading followed by creep during decaying stress in the lower crust? *J Geophys Res Solid Earth* 120(5):3119–3141. <https://doi.org/10.1002/2014JB011708>
- Pearce MA, Wheeler J (2011) Grain growth and the lifetime of diffusion creep deformation. *Geol Soc London Spec Public* 360(1):257–272
- Pennacchioni G, Mancktelow NS (2007) Nucleation and initial growth of a shear zone network within compositionally and structurally heterogeneous granulites under amphibolite facies conditions. *J Struct Geol* 29(11):1757–1780. <https://doi.org/10.1016/j.jsg.2007.06.002>
- Pennacchioni G, Mancktelow N (2018) Small-scale ductile shear zones: neither extending, nor thickening, nor narrowing. *Earth Sci Rev* 184:1–12
- Petley-Ragan A, Dunkel KG, Austrheim H, Ildefonse B, Jamtveit B (2018) Microstructural records of earthquakes in the lower crust and associated fluid-driven metamorphism in plagioclase-rich granulites. *J Geophys Res Solid Earth* 123(5):3729–3746. <https://doi.org/10.1029/2017JB015348>
- Petley-Ragan AJ, Plümper O, Ildefonse B, Jamtveit B (2020) Nano-scale earthquake records preserved in plagioclase microfractures from the lower continental crust. *Solid Earth Discuss* 2020:1–14. <https://doi.org/10.5194/se-2020-146>
- Piazzolo S, Bestmann M, Prior D, Spiers C (2006) Temperature dependent grain boundary migration in deformed-then-annealed material: observations from experimentally deformed synthetic rocksalt. *Tectonophysics* 427(1):55–71. <https://doi.org/10.1016/j.tecto.2006.06.007>
- Pittarello L, Di Toro G, Bizzarri A, Pennacchioni G, Hadzadeh J, Cocco M (2008) Energy partitioning during seismic slip in pseudotachylite-bearing faults (Gole Larghe Fault, Adamello, Italy). *Earth Planet Sci Lett* 269(1–2):131–139
- Prior DJ, Wheeler J, Peruzzo L, Spiess R, Storey C (2002) Some garnet microstructures: an illustration of the potential of orientation maps and misorientation analysis in microstructural studies. *J Struct Geol* 24(6):999–1011. [https://doi.org/10.1016/S0191-8141\(01\)00087-6](https://doi.org/10.1016/S0191-8141(01)00087-6)
- Putnis A (2002) Mineral replacement reactions: from macroscopic observations to microscopic mechanisms. *Mineral Mag* 66(5):689–708
- Putnis CV, Tsukamoto K, Nishimura Y (2005) Direct observations of pseudomorphism: compositional and textural evolution at a fluid-solid interface. *Am Miner* 90(11–12):1909–1912
- Ruiz-Agudo E, Putnis CV, Putnis A (2014) Coupled dissolution and precipitation at mineral–fluid interfaces. *Chem Geol* 383:132–146. <https://doi.org/10.1016/j.chemgeo.2014.06.007>
- Rutter E, Brodie K (1995) Mechanistic interactions between deformation and metamorphism. *Geol J* 30(3–4):227–240
- Segall P, Simpson C (1986) Nucleation of ductile shear zones on dilatant fractures. *Geology* 14(1):56–59. [https://doi.org/10.1130/0091-7613\(1986\)14%3c56:nodszo%3e2.0.co;2](https://doi.org/10.1130/0091-7613(1986)14%3c56:nodszo%3e2.0.co;2)
- Skemer P, Katayama I, Jiang Z, Karato S-i (2005) The misorientation index: development of a new method for calculating the strength of lattice-preferred orientation. *Tectonophysics* 411(1–4):157–167
- Spruzeniece L, Piazzolo S, Maynard-Casely HE (2017) Deformation-resembling microstructure created by fluid-mediated

- dissolution–precipitation reactions. *Nat Commun* 8(1):14032. <https://doi.org/10.1038/ncomms14032>
- Stünitz H, Fitz Gerald J (1993) Deformation of granitoids at low metamorphic grade. II: Granular flow in albite-rich mylonites. *Tectonophysics* 221(3–4):299–324
- Stünitz H, Gerald JF, Tullis J (2003) Dislocation generation, slip systems, and dynamic recrystallization in experimentally deformed plagioclase single crystals. *Tectonophysics* 372(3–4):215–233
- Stünitz H, Neufeld K, Heilbronner R, Finstad AK, Konopásek J, Mackenzie JR (2020) Transformation weakening: Diffusion creep in eclogites as a result of interaction of mineral reactions and deformation. *J Struct Geol* 139:104129
- Svahnberg H, Piazzolo S (2010) The initiation of strain localisation in plagioclase-rich rocks: Insights from detailed microstructural analyses. *J Struct Geol* 32(10):1404–1416
- Wheeler J, Prior D, Jiang Z, Spiess R, Trimby P (2001) The petrological significance of misorientations between grains. *Contrib Miner Petrol* 141(1):109–124
- Xia F, Brugger J, Chen G, Ngothai Y, O’Neill B, Putnis A, Pring A (2009) Mechanism and kinetics of pseudomorphic mineral replacement reactions: a case study of the replacement of pentlandite by violarite. *Geochim Cosmochim Acta* 73(7):1945–1969. <https://doi.org/10.1016/j.gca.2009.01.007>

Publisher's Note Springer Nature remains neutral with regard to jurisdictional claims in published maps and institutional affiliations.